LUND UNIVERSITY
Faculty of Science

Development of a Neutron Activation Analysis Station at the Lund Ion Beam Analysis Facility

Josephine Lindsey-Clark

Thesis submitted for the degree of Bachelor of Science, 15 hp
Project presented: January 2021

Supervisor: Robert Frost
Co-supervisors: Kristina Stenström, Mikael Elfman

Department of Physics
Division of Nuclear Physics
Autumn Semester 2020

Abstract

This report outlines the first stages of the development of the Neutron Activation Analysis station at the Lund Ion Beam Analysis Facility in the Division of Nuclear Physics, Lund University. The motivation for this project is to use the Neutron Activation Analysis detection technique for environmental monitoring around the European Spallation Source, soon to come into operation. In the event of an emergency scenario, some radiotoxic isotopes may be released into the environment from the Tungsten spallation target, including the difficult to detect lanthanide, ^{148}Gd. In normal operation, a variety of radionuclides may also be released. In this initial stage, the aim was to build a measurement station which is able to measure very short-lived activation products, and to investigate if it is possible to trace gadolinium isotopes in environmental samples using neutron activation analysis.

The measurement station was constructed over the span of one semester, and a selection of metal foils and environmental samples were activated and analysed. The samples were irradiated using a portable neutron generator with a maximum production rate of $4.71 \cdot 10^8$ n/s. Two methods of measurement were utilised: one which used irradiation- and measurement-times of longer than one hour, and another which used a fast pneumatic transport system with irradiation- and measurement-times of less than 1 minute. High Purity Germanium detectors were used to measure the γ-rays emitted from the activated samples. Results showed that with the selection of tested samples, it was possible to measure activation products with half-lives as short as two seconds using the fast pneumatic line. In the environmental samples, it was seen that amounts larger than several grams were needed in order to see activation and that longer irradiation time was more suitable. The results obtained show that the station has the potential to be developed for use with the Compact Accelerator-driven Neutron Source under development at the facility, which is anticipated to achieve a neutron production rate of 10^{11} n/s.

Contents

List of Figures

List of Tables

List of Abbreviations

BAR	Biospheric and Anthropogenic Radioactivity
CANS	Compact Accelerator Neutron Source
CPS	Counts Per Second
DAQ	Data Acquisition System
DD	Deuterium Deuterium
DT	Deuterium Tritium
ESS	European Spallation Source
HPGe	High Purity Germanium
LEPS	Low Energy Photon Spectrometre
LIBAF	Lund Ion Beam Analysis Facility
LINAC	Linear Accelerator
MCA	Multi Channel Analyser
NAA	Neutron Activation Analysis
NG	Neutron-Generator
NUANS	Nagoya University Accelerator-driven Neutron Source

1 Introduction

The purpose of this project was to initiate the construction of a new Neutron Activation Analysis (NAA) measurement station at the Lund Ion Beam Analysis Facility (LIBAF), Lund University. The motivation for this project was to use NAA to perform environmental monitoring around the European Spallation Source (ESS), soon to begin operation. NAA is a nuclear technique which uses a neutron source to irradiate a chosen sample, transforming the isotopes contained into γ-ray emitters. The γ-ray emissions from the sample can then be studied, so that the isotopic contents may be identified by their known characteristic spectra. If the reaction cross section, neutron flux, detector efficiency, irradiation time and measurement time are known, this technique is fully quantitative. Once established, the NAA station will improve the capabilities of Lund University to monitor the environment surrounding ESS and compare the condition before and after operation commences.

1.1 Background

The Biospheric and Anthropogenic Radioactivity (BAR) group at the Division of Nuclear Physics, Lund University, investigates man-made radionuclides found in the environment. LIBAF, in the same division, uses ion-beam analysis techniques for material composition analysis. In order to advance the current capabilities at Lund, their intention is to investigate the possibility of using NAA for detecting radionuclides in the environment, produced by ESS.

The most common neutron source used for NAA is a nuclear reactor, where the sample is placed in an irradiation chamber and must then be transported to an analysis facility. This means that any radionuclides with short half-lives of less than an hour are unlikely to be successfully measured. Nuclear reactors suitable for activation are declining in number, meaning that the technique is becoming less prevalent and therefore more expensive [1]. This issue is being countered by a growing interest in Compact Accelerator-drive Neutron Sources (CANS), such as the one under construction at LIBAF, which will operate by impinging a 2.5 MeV deuteron beam into a beryllium target. Neutron-generators (NGs), with a production rate in the order of 10^8 n/s, may also be used. Compared to a reactor with a typical production rate of 10^{16} n/s, NG flux is relatively small, but activation is usually still possible. The portable NG at LIBAF can be run in the laboratory in immediate proximity to the analysis station.

1.2 Motivation

Within the coming years, the most powerful pulsed neutron source in the world, ESS, is due to begin operation [2]. While running, an intense beam of high-energy protons directed onto a large tungsten target will produce neutrons from spallation, as well as a great variety of radioactive byproducts. A small portion of these will be released into the surroundings

during normal operation, while in the event of an accident, a great variety of gases and aerosols may additionally be released. The range of radionuclides generated in this scenario will be unique from existing sources such as power plants and other accelerators [2], creating the need for new identification methods. From research conducted at Lund University [3], it was found that for several ESS radioactive by-products, there is no published method for their analysis in the environment. In particular, the radiotoxic lanthanide ^{148}Gd is highlighted as the most important to detect in an accident scenario. This is due to it being an α-particle emitter with high dose coefficients for the public, of $5.6{\cdot}10^{-8}$ for ingestion and $2.6{\cdot}10^{-5}$ for inhalation, and a half-life of 75 years. ^{148}Gd has so far been difficult to analyse in previous studies conducted by Lund University and ESS, and improved techniques for its detection are required.

The Swedish Radiation Safety Authority requires that the annual effective does to the public from ESS must not exceed 0.1 mSv per year [3]. A project carried out by Lund University and ESS has implemented several techniques to establish the current levels of ionising radiation and concentration of various radionuclides, natural and artificial, in the surroundings of ESS prior to the beginning of operation. The techniques used for this study included γ-ray spectroscopy, accelerator mass spectrometry, inductively coupled plasma mass spectrometry and liquid scintillation counting [4]. For most of these techniques, pre-separation is usually required before analysis. This means they are useful for long-lived radioisotopes, but after performing necessary treatment prior to measurement, short-lived radionuclides will have already decayed. NAA is commonly used for environmental monitoring [5] [6] [7] to detect metals in soil, water or sediment. In many cases, pre-separation and pre-concentration may also be needed, but because this is done prior to activation, this process does not affect the time delay to measurement. By constructing a NAA station where analysis is performed directly after activation, the number of isotopes which can be detected is increased.

1.3 Report Structure

This report first outlines the key theoretical concepts behind NAA, including neutron sources and neutron and γ-ray interactions with matter. The construction of the measurement station is then described, followed by a presentation and discussion of the results. A final summary and future outlook are given in the concluding chapter.

2 Theory

NAA was first developed in 1936 [8], when it was observed that particular rare earth elements became highly radioactive after being exposed to a neutron source. It has since proven to be useful in any circumstance where quantitative knowledge of the composition of a material is needed. This chapter outlines the basic principles of NAA, the fundamentals of the neutron and the associated topics of neutron production and γ-ray detection.

2.1 Neutron Activation Analysis

The use of NAA is advantageous over other analysis techniques for a number of reasons. Firstly, NAA allows isotopes to be sampled discretely, by focusing only on the nucleus and therefore not destroying the sample in the process of analysis. Traditional chemical techniques can often involve dissolving, vaporising or burning the sample to analyse it [9]. The accuracy of NAA is highly variable, depending on the setup and detector used and the particular element and isotope measured. Detection limits can be in the order of ppm [10], and in the case of Ir, as low as ppt [11]. NAA is not sensitive to about one third of elements because no radioactive product can be created [2].

For a given neutron source, the neutron field [1], ϕ is given by:

$$\phi = \frac{A}{\sigma \cdot \lambda}, \tag{2.1}$$

where σ is the reaction cross section, A is the activity of particular activation product, and λ is the decay constant. A can be determined using:

$$A = \frac{N}{\epsilon \cdot P_\gamma \cdot t_c}, \tag{2.2}$$

where ϵ is the efficiency of the detector, P_γ is the branching ratio for γ-ray emission, t_c is the measurement time and N is the number of activation product atoms. N is both growing and decaying during activation [12]. The number of atoms at a given irradiation time, t, is given by:

$$N(t) = \frac{R}{\lambda} - \left(\frac{R}{\lambda} - N_0\right) e^{-\lambda t}, \tag{2.3}$$

where N_0 is the number of existing atoms at the beginning of irradiation (t=0), R is the reaction rate and is dependent on the number of target atoms in the sample N_s, given by [12]:

$$R = N_s \sigma \phi. \tag{2.4}$$

Once activation is stopped, the activation product atoms only decay, according to:

$$N(t) = N_0 e^{-\lambda t}. \tag{2.5}$$

2.1.1 Neutrons and Isotopes

The discovery of the neutron in 1932 [13] was a turning point in the scientific understanding of the nucleus. This followed after James Chadwick performed a series of experiments on beryllium and boron samples, bombarding them with α-particles from polonium. The neutron was immediately used as a new probe for nuclear structure, resulting in several new discoveries. These included the creation of previously unknown isotopes and radioactive elements through neutron irradiation [14], as well as nuclear fission [15], all within the same decade.

Nuclear binding energy is the minimum energy that would be needed to disassemble a nucleus into its constituent nucleons. It represents the energy required to work against the strong nuclear force holding them together, quantified by the difference between the nucleus and the masses of the collective individual nucleons. This mass difference is known as the mass defect. The liquid drop model [16], describes the nucleus as a fermi-liquid made up of neutrons and protons. The model is able to reproduce the main features of the nuclear binding energy, E_B, of nuclei by the Bethe-Weizsacher formula:

$$E_B = a_v A - a_s A^{2/3} - a_A \frac{(A-2Z)^2}{A^{1/3}} - a_c \frac{Z(Z-1)}{A^{1/3}} + a_p \frac{\delta}{A^{1/2}}, \tag{2.6}$$

where a_v, a_s, a_A, a_C and a_P are fit coefficients accounting for volume, surface, area, coulomb effect and pairing, and are dependent on the data used. When A,Z is even, δ is positive, when A,Z is odd, δ is negative, and where A is odd, δ is 0. The form of the surface and asymmetry terms imply that neutrons are required to stabilise nuclei and that stability requires a high A/Z ratio as A increases.

Continued experiments revealed that nuclear binding energy showed significant systematic deviations from those calculated by the liquid drop model [17] [18]. In particular, some nuclei had higher binding energies for particular numbers of nucleons, suggesting that at certain atomic numbers, nuclei were more tightly bound together. This gave way to the idea that the nucleus may be constructed in 'shells' [19], analogous to bound electrons, where nucleons occupy sets of discrete energy levels within the nucleus. How full each of these levels is affects the binding energy of that nucleus, where those with full shells become singly or doubly 'magic'. Nuclei with a full outer shell of protons *or* neutrons (singly magic), or protons *and* neutrons (double magic) are very tightly bound and thus have much higher binding energies. This has the effect that the energy required to excite such a nucleus, where a nucleon is moved to a higher unoccupied energy level, is exceptionally high. This is because the next highest energy level lies in the next shell, across a large energy gap of several keV. The understanding of magic numbers is essential in determining how a particular nucleus will interact with matter, including other nuclei, neutrons and other radiation [20].

2.1.2 Neutron Interactions with Matter

Neutrons are neutral particles which interact only by the strong nuclear force; as such, they are highly penetrating into matter and interact directly with nuclei. Neutrons may interact via elastic and inelastic scattering with nearby nuclei, or be absorbed by neutron capture [21]. Absorption results in the formation of a compound nucleus, which can trigger the production of β±-decay, α-particle emission, or fission [22], all of which have the potential to result in γ-ray emission. The extent to which neutrons interact with nuclei is described by cross-sections, (σ), describing the probability of a particular interaction between an incident neutron and a target nucleus. The cross-section can be interpreted as an effective 'target area', given in barns (b), equivalent to 10^{-24} cm^2. The cross section is energy dependent, and generally increases exponentially with reducing energy. Fig 2.1 shows examples of the total reaction cross sections for ^{158}Gd(n,total), ^{115}In(n,total), ^{93}Nb(n,total), ^{58}Ni(n,total) and ^{27}Al(n,total), between neutron energies of 10 μeV and 20 MeV. Data was obtained from the JEFF 3.3 data file using the IAEA JANIS database [23].

The neutron cross section is specific to each nucleus. The peaks seen in 2.1 are caused by resonances [24], relating to the nuclear structure of the target nucleus. The excitation energy of the compound nucleus formed after neutron capture is the sum of the mass deficit of the formation reaction and the kinetic energy of the neutron. The recoil energy can be ignored because of the far greater mass of the nucleus relative to the neutron. If the energy of the neutron is such that a compound nucleus can be formed at one of the excitation states, this causes a resonance.

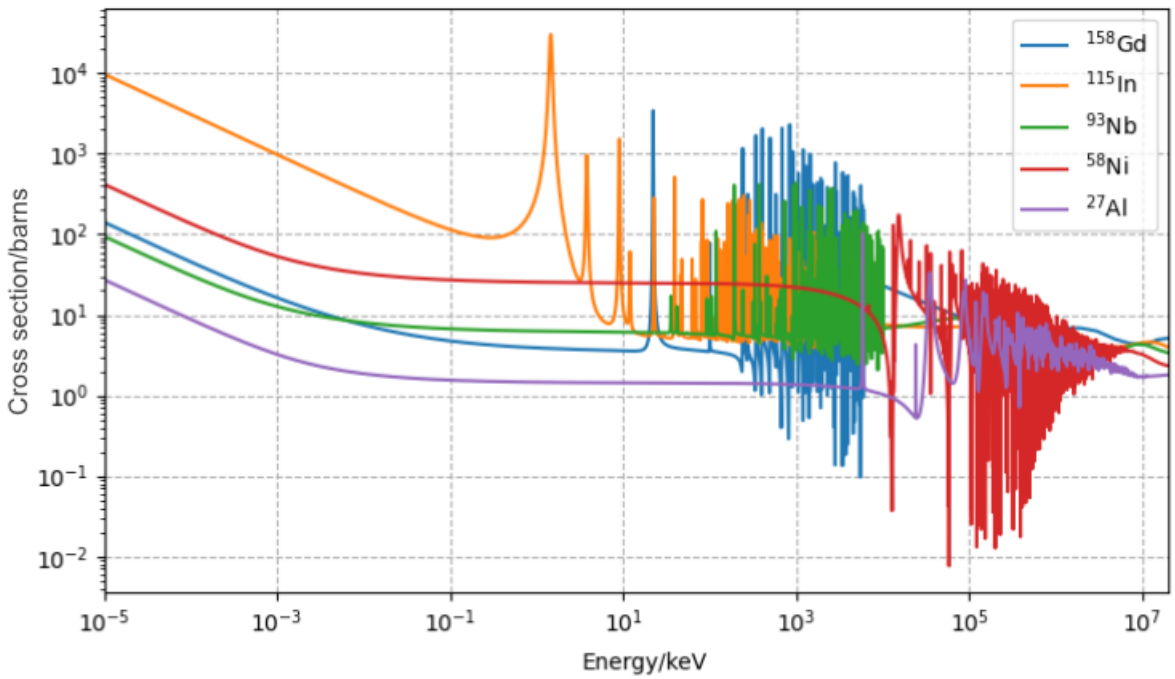

Figure 2.1: Energy dependent total neutron interaction cross sections for the most abundance isotopes of ^{27}Al, ^{58}Ni, ^{93}Nb, ^{115}In, ^{158}Gd.

2.2 Neutron Sources

Nuclear reactors have been the preferred neutron source for NAA, owing to their very high neutron production of up to 10^{17} n/s. Significantly lower production of 10^6 n/s can be achieved with several different types of radioactive sources [3], including ^{252}Cf, which produces neutrons from spontaneous fission, and polonium-berylium or plutonium-berylium sources, which produce neutrons from the ^{9}Be(α, n)^{12}C reaction. CANS are additional alternatives to reactor sources [25]. In CANS, an accelerator produces a particle beam, which is directed to one or more compact target stations to produce neutrons. The neutrons then enter the beam lines, and can be used for multiple simultaneous experiments. Current facilities include NUANS [26] at Nagoya University, Japan and SONATE [27] in France.

Neutrons can be produced with NGs by the DD d(D,^{3}He)n (at 2.5 MeV) or the DT d(T,^{3}He)n (at 14.1 MeV) reactions [4]. DD NGs contain no radioactivity, meaning they are not a radiation hazard when turned off. However, DT NGs must be sealed because they contain tritium with a half-life of 12.3 years [28]. The lifetime of DT NGs is limited by their tritium content, making their typical lifespan in the order of a few thousand hours, where the neutron flux continually decreases.

DD NGs have the advantage that neutron cross sections tend to be much greater at lower energies, and they are considered to be safer because they are not inherently radioactive [1]. The neutron yield, however, is typically far less than that produced with the DT reaction. This is because the DD reaction cross-section itself is much lower, and their neutron output is therefore only around 1% of DT generators.

Neutron production by spallation sources [29] requires a high energy proton beam of 1 GeV or higher to be focused onto a target of heavy metal. This produces neutrons at very high power and brilliance. There are several spallation sources around the world with a variety of different production methods and neutron yields. The ISIS neutron source [30] in Oxfordshire, for example, accelerates protons using a combination of linac and synchroton on to a lead target, producing neutrons and muons. ESS [29] will use a linac to accelerate protons onto a Tungsten target, creating the highest brilliance neutron source ever constructed.

2.3 γ-Rays

2.3.1 γ-Ray Interactions with Matter

γ-rays are penetrating high energy photons, which result from the relaxation of a nucleus from one excited state to a lower excited state or ground state [31]. The energy of the photon is equal to the difference in energy of those discrete energy levels, and is therefore indicative of a specific transition within a specific nucleus, characterised by its shells. These transitions usually occur within 10^{-12} seconds. After a radioactive decay, a γ-ray 'cascade' may be observed, when the nucleus transitions through multiple states to reach the ground state, each time producing a γ-ray. Sometimes, one of these intermediate states may be more stable than average, and is known as metastable, existing several orders of magnitude longer. These metastable states are called isomers and are much easier to measure due to their longer half-lives.

The three main ways in which γ-rays interact with matter are through the photo-electric effect, Compton scattering and pair production. The photo electric effect occurs when a

γ-ray is absorbed by an atom, exciting one of its electrons. The relationship between the energy of the γ-ray, (E_γ), and the kinetic energy given to the electron is expressed as:

$$E_\gamma = hf = \phi + K_e, \tag{2.7}$$

where h is the Planck constant, ϕ is the work function of the material and K_e is the kinetic energy of the electron. This is observed at lower energies, dependent on the atomic number of the atom in which the γ-ray was produced. Compton scattering becomes more dominant at mid-range energies, because the energy of the photon becomes too great for absorption. Compton scattering [32] is the process where a photon meets a charged particle and transfers part of its energy to the particle, resulting in a decrease in frequency and change in direction of the photon, and recoiling of the particle. The change in energy of the photon can be found by calculating the change in wavelength, expressed by:

$$\lambda' - \lambda = \frac{h}{mc}(1 - cos\ \theta), \tag{2.8}$$

where m is the mass of the charged particle, θ is the scattering angle, and λ is the wavelength of the photon. At energies greater than 1022 keV, pair production becomes possible. Here, an electron-positron pair is spontaneously created from a γ-ray with energy greater than twice the electron rest mass (m_e), 511 keV, in the presence of a strong electro-magnetic field, usually from a nearby heavy nucleus. The resulting positron annihilates shortly afterwards when it meets an electron, and two γ-ray photons, each with an energy of 511 keV are created. The energy of the annihilation pair is given by:

$$2K_e = E_\gamma - 2m_e c^2, \tag{2.9}$$

where c is the speed of light.

2.3.2 γ-Ray Detectors

The most common detectors used in NAA are semiconductor detectors and scintillator detectors. The High Purity Germanium (HPGe) detector is a solid state crystal with a p-n junction [33]. The p-n doping forms a depletion region that detects incident radiation by the presence of electrons and holes, generated by a γ-ray photon depositing its energy into the detector crystal. Scintillator detectors [34] based on materials such as sodium iodide and lanthanum bromide, create scintillation light, generated by relaxation of electrons after the incoming radiation has excited them into a higher energy state. What distinguishes the HPGe detector [35] from scintillators is the significantly higher energy resolution. The higher resolution is due to the lower band gap in germanium of 0.7 eV, compared to a sodium iodide scintillator of 5.9 eV. This means that for each incident γ-ray, the HPGe produces almost ten times the number of electron-hole pairs, creating a higher current pulse.

Before entering the detector many photons will undergo Compton scattering in the surrounding material [36]. Event counting in the detector is based on the photopeak, where the photopeak efficiency reduces with increasing energy. In γ-γ coincidence measurements, two or more γ-rays, which are emitted almost simultaneously, are detected by two detectors. Using the coincidence technique, both γ-rays are detected, which is useful in reducing background noise [37].

3 Methodology

This chapter first describes the LIBAF NG and the geometry of the surrounding 'cave'. Following this, three different setups are presented: measurement inside the cave with a single detector, long term measurements with a low energy photon spectrometer (LEPS) detector, and a fast pneumatic transport system with two detectors configured for coincidence measurements. Lastly, the samples and sample preparation are presented.

3.1 LIBAF Neutron Cave

Fig 3.1 shows a schematic diagram of the NG. The vacuum enclosure is a sealed container enclosing the radioactive tritium. The replenisher pressurises the tube by heating the deuterium and tritium gas mixture. The ion source ionises the gas mixture, forming plasma, from which ions are then extracted. The ions are focused into a beam through, the acceleration region by a potential of 120 V. Finally, the ions then hit the hybrid deuterium tritium target, producing neutrons. The entire system is enclosed by a stainless steel container filled with SF_6 gas at a pressure of 4-5 bar, which provides dielectric rigidity needed to operate at a very high voltage [38].

Fig 3.2 shows a simulation of the geometry of the area surrounding the NG, created in GEANT4 [39]. The surrounding cave is heavily shielded with water containers and sheets of borated polyethylene, while the door is shielded with borated polyethylene only. The NG is surrounded by a plastic cylinder of radius 55 mm, contained in a larger cylinder, filled with distilled water, of radius 225 mm. Fig 3.3 shows the simulated neutron energy spectrum produced within the cave, using $6 \cdot 10^6$ neutrons. The neutrons are emitted isotropically with a normal distributed energy, where the mean corresponds to the maximal neutron energy from T(d,n)^{4}He at E_d=120 keV. The tritium content is 120 GBq [38].

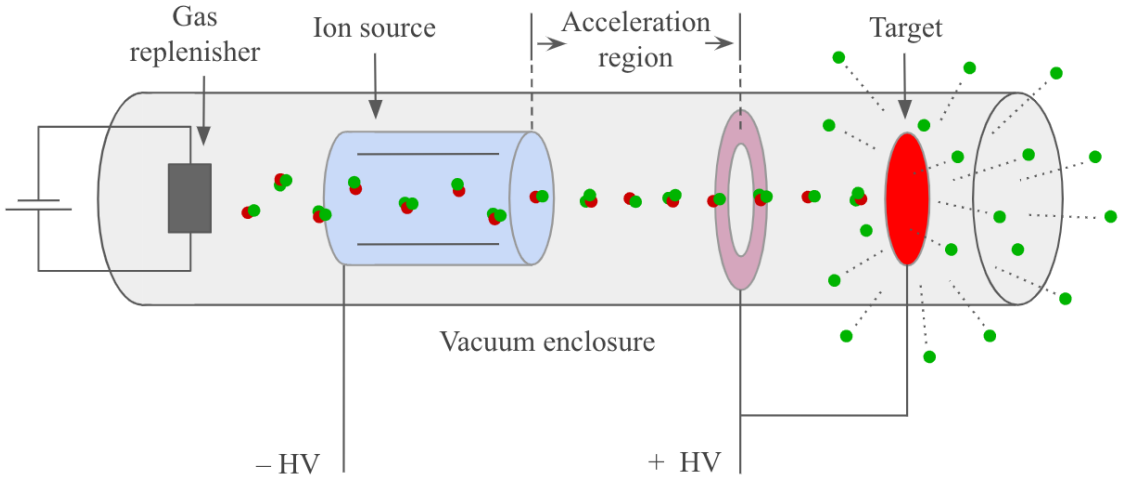

Figure 3.1: Schematic diagram of the Genie 16 Sodern NG.

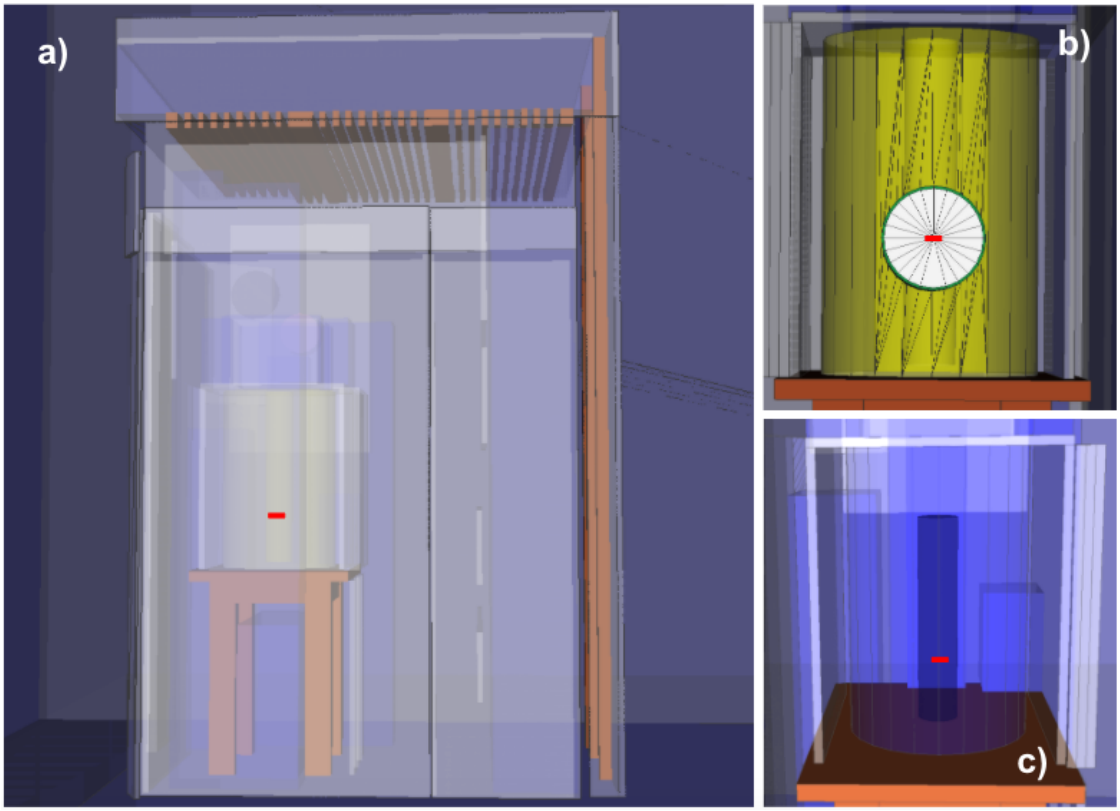

Figure 3.2: Simulated geometry of the LIBAF neutron cave: a) shows the area surrounding the NG, including the shielded cave, door and table underneath. b) shows the exit port on the opposite side, protruding from the 225 mm cylinder. c) shows the 55 mm cylinder encasing the NG. The target is shown in red, and is approximated to be in the centre of this inner cylinder. The target is marked on all the images for reference.

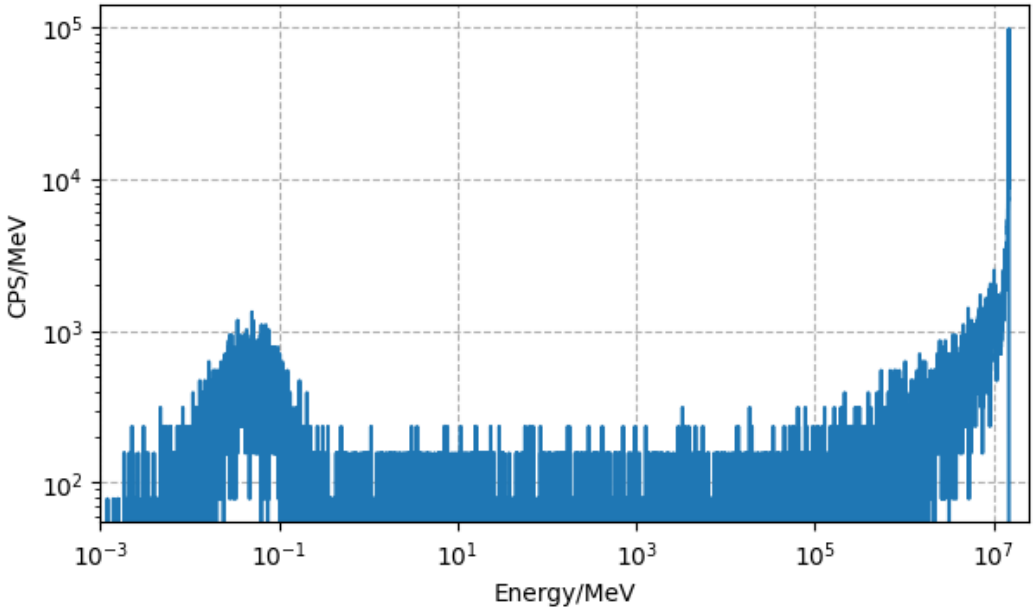

Figure 3.3: Neutron energy spectrum simulated in GEANT4, based on 6 million neutrons. The CPS have been scaled to $4.7{\cdot}10^8$ n/s in this plot. This represents the neutron energy distribution hitting the plane at the end of the exit port at a distance of 22.5 cm from the target. The circular area enclosed by the perimeter of the exit port is 340 cm^2.

There are several safety features which ensure the NG can be operated safely. For example, a built-in safety loop is used as emission zone access control, where the NG will turn off if the door to the surrounding enclosure is opened. This stops neutron emissions by cutting the voltage to the gas replenisher and the ion source. A red light on the cave turns on when neutrons are being emitted. As well as this, the surrounding area of the lab must be closed off with a barrier, such that the dose received, approximately 120 μSv/h, is at least 25 times less than at the neutron source. Since the dose rate is inversely proportional to the square of the distance, this is achieved at a distance of 5 metres. Neutron and γ-ray detectors with live dose rate displays are placed approximately one metre away from the cave.

3.2 Detector Setup Inside Neutron Cave

To measure the activity inside the neutron cave with the NG switched on and off, a HPGe detector was placed approximately 10 cm from the neutron source in both shielded and unshielded configurations. Cadmium sheets were used for shielding due to its high cross section with thermal neutrons, approximately $10^4 - 10^6$ barns. The sheets were wrapped in plastic bags and handled with gloves to prevent coming into contact with any residue. Plastic was also used to slow the neutrons to energies that would be absorbed by the cadmium, preventing them from reaching the detector. The detector was placed in the same position in both configurations. Surrounding this, the setup was heavily shielded with at least 20 cm of lead on all sides. Fig 3.4 a) shows a schematic representation of the shielded configuration.

3.3 Long-term Irradiation and Measurement

At the closest point to the neutron target (a distance of 55 mm), a thin sheet of plastic holding four foils of aluminium, indium, nickel and niobium was positioned at the end of a collimator, as shown in Fig 3.4 b) and c). The collimator was used for another experiment

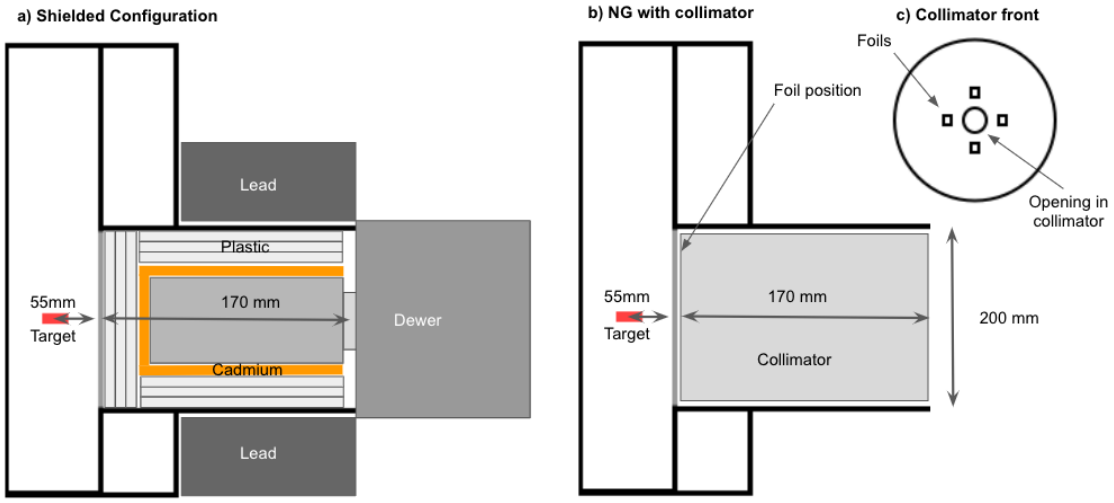

Figure 3.4: Geometries of the experimental setups used inside the LIBAF neutron cave: a) shows the shielded configuration used to take measurements from inside the cave. b) shows the configuration used during long term irradiation, and c) shows a front view of the four foils positioned at the end of the collimator

Table 3.1: NG run times for long-term irradiation of the foils.

Generator	Minutes	Day	n-production rate (n/s)
ON	3	1	$8.20 \cdot 10^7$
ON	16	1	$8.00 \cdot 10^8$
ON	91	1	$4.45 \cdot 10^8$
OFF	**78**		
ON	5	1	$2.80 \cdot 10^8$
ON	9	1	$3.50 \cdot 10^8$
ON	5	1	$4.50 \cdot 10^8$
ON	221	1	$4.70 \cdot 10^8$
OFF	**902**		
ON	1	2	$3.20 \cdot 10^8$
ON	21	2	$3.50 \cdot 10^8$
ON	532	2	$4.70 \cdot 10^8$
OFF	**865**		
ON	21	3	$3.00 \cdot 10^8$
ON	390	3	$4.70 \cdot 10^8$
OFF(cooling)			

conducted by researchers visiting from Uppsala, but served to hold the foils in place in this parasitic experiment. The foils were irradiated in this position intermittently over 3 days, after which the NG was stopped, and the activity of the sources was measured with a dosimeter following a 10 minute cooling period. Table 3.1 displays the irradiation times. The four foils were measured individually by placing each one in a petri dish and setting on top of the LEPS detector, approximately 2 cm above the detector window. The foils were each later remeasured for several hours.

The LEPS detector, model GMX-23190-P, had a thin beryllium window, increasing the resolution of measurements. The detector was biased by a HV power supply set at -2,500 V, Ortec model 659. The spectroscopy amplifier and gated integrator used, Ortec model 673, was set with a coarse gain of 100, a fine gain of 40 and a shaping time of 2 µs. The spectra were acquired using a single input multi-channel analyser (MCA) with 8000 channels, made by Ortec. The MCA data was read by the software package Maestro, and then saved in ASCII format for analysis in Python.

The experiment ran over a total of 52 hours and 40 minutes, with an additional cooling time of 46 minutes between the generator being turned off and the first Indium measurement being started. The NG was on for 21 hours and 55 minutes, where the average production rate over this time was calculated to be 4.65 $\cdot 10^8$ n/s.

3.4 Pneumatic Transport System Design

3.4.1 Construction of the Transport and Analysis System

To reduce the time between irradiation and measurement of samples, a new measurement station was constructed outside of, but in close proximity to the neutron source. Two detectors were used in this analysis station, both increasing the solid angle and adding the

possibility to perform γ-γ coincidence measurements. To transport the sample, a pneumatic transportation line was built with solenoid valves controlled by a switch to vary the direction of travel of an aluminium sample holder. The pneumatic line ran from directly in front of the neutron source, and was fed through a small opening in the back of the surrounding cave to the analysis station. A schematic representation is shown in Fig 3.5 a).

Fig 3.5 b) shows the two HPGe detectors arranged to record γ-rays from the sample. The distance from the centre of the pipe to the end of the detector head is 4.5 cm in both cases. The aim of this arrangement was to position the section of the pipe holding the sample as close as possible to both the detector crystals in the centres of the detector heads. Because the path from the source to the detectors had several bends, a spiral reinforced hose was used to prevent it from losing shape and jamming the sample holder. The inner diameter of the hose was 25 mm and the outer diameter of the sample holder was 22 mm. The sample holder was wrapped in electrical tape so that it would fit the hose and was lubricated with vacuum grease.

The transport line was terminated at each end by two pieces of steel pipe of the same diameter as the hose, each threaded at one end. The ends of the hose were warmed with a heat gun so that the unthreaded ends of the pipe could be inserted into the hose. These were held in place using jubilee clips to prevent the pipe from being forced out under high pressure. The threaded ends were connected to the pneumatic supply lines. 3D printed fittings were designed in FreeCad to ensure the sample would rest in a set position at the detectors and neutron source.

To change the direction of travel, a combination of four solenoid valves was used: one inlet and one outlet valve for each end of the line. The solenoid valves were wired to a three-way ON-OFF-ON switch located at the desk along with the NG control panel and PC setup for viewing live spectra. In each ON configuration, one inlet and one outlet valve was open at each end of the line. In the OFF configuration both inlet valves were closed and both outlet valves were open. A high flow rate pneumatic line was used to supply the system with 7 bar air pressure.

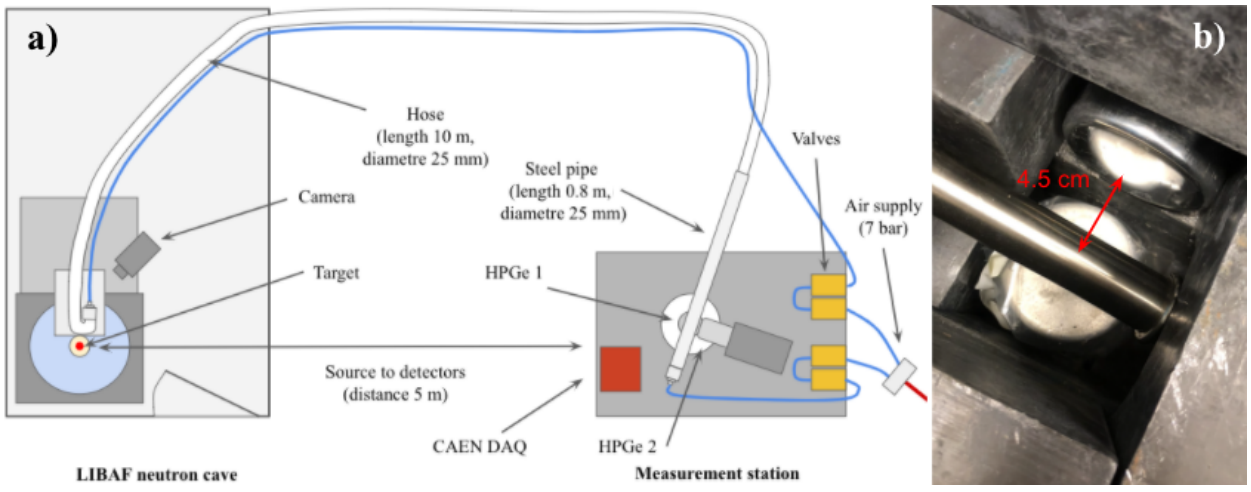

Figure 3.5: Experimental setup used for short-term irradiation: a) top down schematic of the setup, not to scale b) HPGe detector heads arranged to measure the sample resting in the pipe, both of which are Canberra model GC2018, placed equidistant from the sample position.

3.4.2 Data Acquisition Systems

Two DAQs were tested for use with this setup: CAEN VX1751 and CAEN DT5780.

The CAEN VX1751 is a full signal digitiser with 8 channels sampling at 1GS/s (4 at 2GS/s), and 10 bit resolution. This was connected to the DAQ PC through an optical fiber connection, CONET2, using a A3818 PCIe card, also made by CAEN. Jadaq software was used to configure the digitiser, acquire the data and store it in HDF5 binary format. The system had 1 Vpp input range, 16-bit programmable DC offset adjustment: ±0.5 V / ±0.1 V. Both trigger-time stamps and global-time stamps were available. The digitiser had a memory buffer of up to 14.4 MS/ch (28.8 MS/ch at 2 GS/s). Data was stored onto a 4TB HDD (WDC_WD40EZRZ) with a 6.0 Gbps SATA link.

The CAEN DT5780 dual digital MCA has two digitiser channels with 14 bit resolution which run at 100 MS/s, and a dynamic range of up to 9.6 V. It can act both as a waveform digitiser or an MCA with all gain settings, trigger thresholds and trapezoidal filter parameters accessible from the MC^2 user interface. The DT5780 is also equipt with two preamp power supply channels and two HV outputs to provide detector biasing up to ±5 kV. The high voltage outputs are also configurable through the MC^2 software, including the ramp-up ramp-down rates. Optical links are available on this also, but for this set up a USB connection was used. List mode outputs, energy and time stamp, and coincidence and anti-coincidence settings between the two channels were also fully configurable within the software.

3.5 Samples/preparation

The Gadolinium and environmental samples were provided by the BAR group at Lund University and the Environmental Radiology and Emergency Preparedness Group at Medical Radiation Physics in Malmö. Several hundred grams of each were put into separate bags and placed at a distance of approximately 20 cm from the target. They were irradiated on separate occasions for several hours, and after a short cooling time, were transported by hand to be measured at the LEPS detector. Several short measurements were taken, followed by a longer final measurement lasting up to 24 hours. The exact sample masses, irradiation and measurements are presented in Table 3.2.

To prepare the samples to be compatible with the pneumatic transport system, they were compressed to fit inside the sample containers. The soil sample was in the form of a fine, dry powder. This was placed into a small bag of known weight, and then packed into the sample holder using the force of the container top to compress it. To maximise the chances

Table 3.2: Masses of each of the samples used in both long and short term measurements.

Sample	Mass in grams (long)	Mass in grams (short)
In	0.840	0.3475
Ni	0.141	0.0730
Nb	0.518	0.2555
Soil	112.975	2.5319
Seaweed	153.933	5.2590
GdO	-	0.5309

of seeing activation products, it was ensured that as much mass as possible was packed into the sample container. This was done by adding a small amount of purified water to dry seaweed, which was then placed into a bag in the sample container. A rod with diameter similar to the container was placed in the opening, and then placed in a vise and tightened. This was repeated until the sample holder was full.

The gadolinium sample was in the form of pure gadolinium oxide. This was placed in a bag in the sample holder to hold it in place to minimise changes in position between different measurements. The foils were also placed in a bag to maintain their position within the sample holder. Aluminium was excluded because the sample holder was made from aluminium. Once the sample under investigation had been placed into the near end of the pneumatic transport system, the NG was turned on. The sample was then sent back and forth between the neutron source and the detectors 6-10 times at 30 second intervals.

4 Results and discussion

This chapter presents and discusses the results acquired from the inside cave, long-term and fast pneumatic transport line configurations. Additionally, a comparison of the experimentally obtained count rates is made to those calculated from theory.

4.1 Detector Setup Inside Neutron Cave

Fig 4.1 shows measurements taken directly after the NG was turned off. Several peaks can be seen corresponding to activation products in the HPGe detector crystal as well as other materials in the cave, including in aluminium, lead and iron. Likely candidates for the major peaks have been identified by comparison with values from literature [40]. It is possible that the cadmium shielding introduced a peak at 247 keV. The average CPS in the measurements taken at 02:34 unshielded and at 2:00 shielded are 5665 and 9025 respectively. The spectra shows a slight reduction noise at higher energies when shielded, however it was decided the level of activation in the cave was too high to continue measurements inside. The risk of neutron damage to the detector was also a concern.

4.2 Long-term Irradiation with LEPS Detector

4.2.1 Detector Calibration

Energy and relative efficiency calibration was provided [41] for the LEPS detector. The calibration used a ^{152}Eu source and reference data taken from [23]. Eleven peaks spanning 100-2000 keV were identified and Gaussians were fitted to find the centroids and areas. 4.2.

The linear fit for the energy calibration and the polynomial for the efficiency are mostly well fitted to the data points. The efficiency of the detector declines at higher energies, which can be seen in the spectra in Figs. 4.1, 4.3, 4.4 and 4.5, which are not efficiency corrected. The steep rise in the fit towards 0 in the efficiency is caused by the detector cutting off at 100 keV, meaning there are no data points, and the fit is therefore not reliable below this energy.

4.2.2 γ-Ray Spectra

Fig 4.3 shows the spectra from long term irradiation of the indium foil. Of the four foils, indium showed the most activation, with ten strong peaks corresponding to the decay of ^{116m}In with a half life of 54 minutes. In the second measurement, a small peak appears at 336 keV from the decay of ^{115m}In with a half life of 4 hours. The third measurement was taken the following day where the activity is significantly lower. The ^{116m}In peaks have all disappeared, while the ^{115m}In peak has become more prominent as background has reduced,

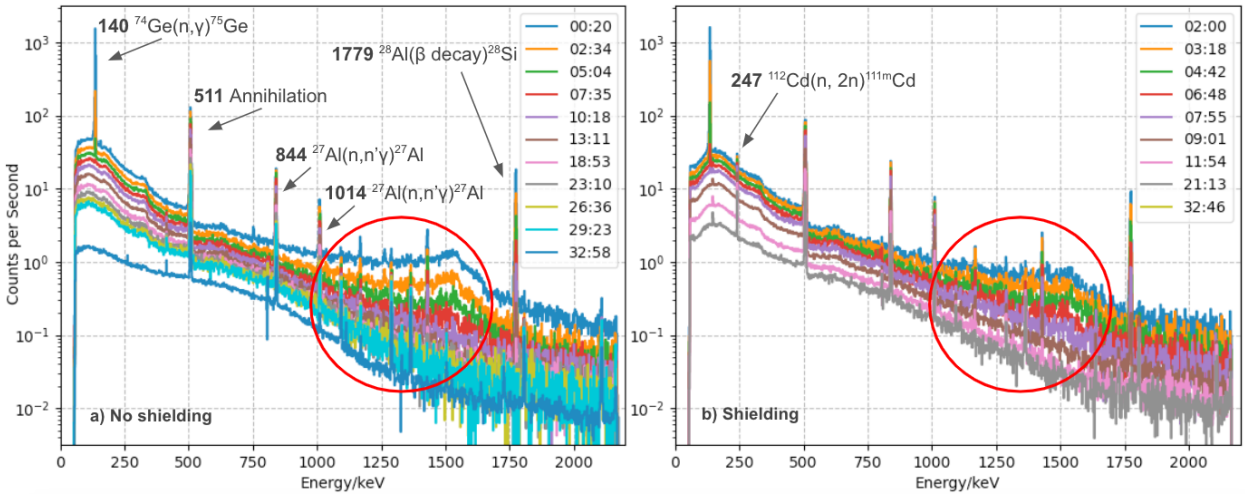

Figure 4.1: Measurements taken with the detector placed inside the cave, where the detector crystal is approximately 15 cm from the target: a) has no shielding and b) is shielded. The legend shows the time the measurement began in minutes and seconds, relative to when the generator was turned off. The red circles highlight a reduction in peak intensity in the shielded configuration. Possible reactions for the strongest peaks present in both unshielded and shielded spectra are labelled in a). In b) a peak appears at 247 keV, which may be a result of the cadmium shielding.

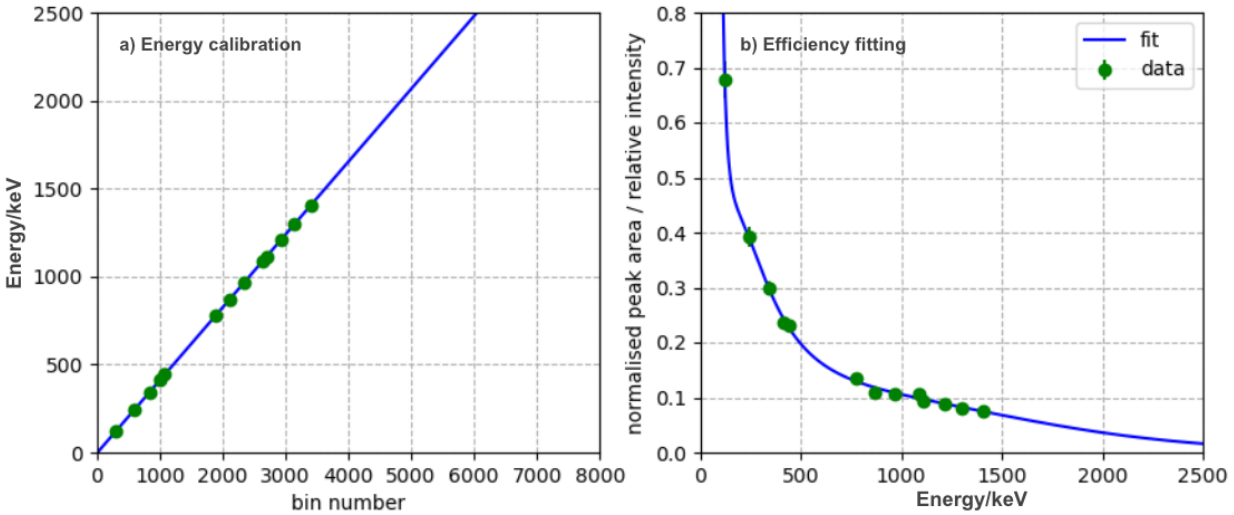

Figure 4.2: LEPS detector calibration. a) Energy calibrated using a linear fitting, error bars are smaller than markers for data points. b) Efficiency fitted with a seventh order polynomial in a loglog scale. Reference energies and intensities taken from ENSDF [23], calibration performed and provided by [41].

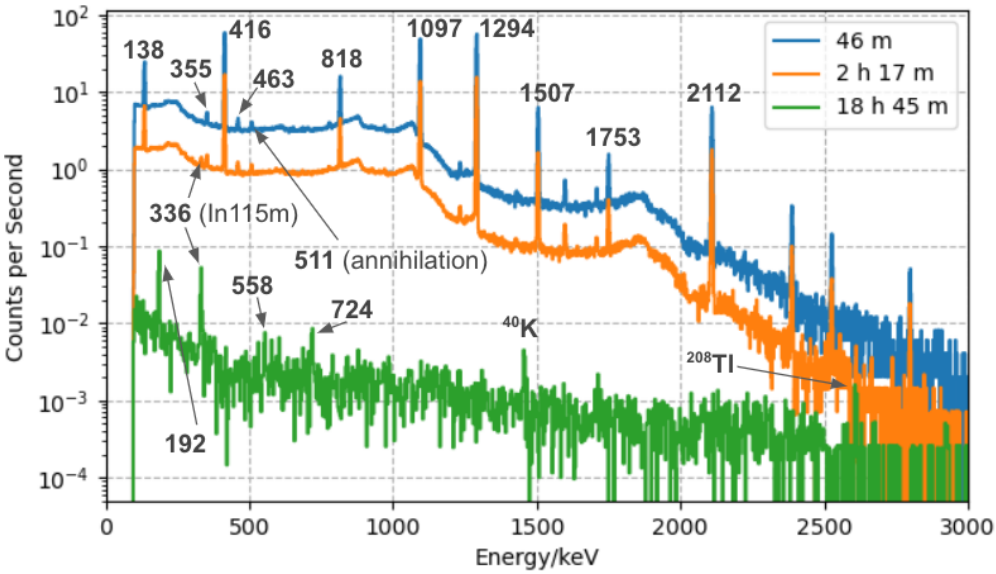

Figure 4.3: Indium measurements taken with the LEPS detector at 46 m, 2 h 17 m and 18 h 45 m after irradiation, showing decreasing activity over time. To reduce statistical fluctuations, each spectrum has been rebinned from 0.4 keV/bin to 1.2 keV/bin.

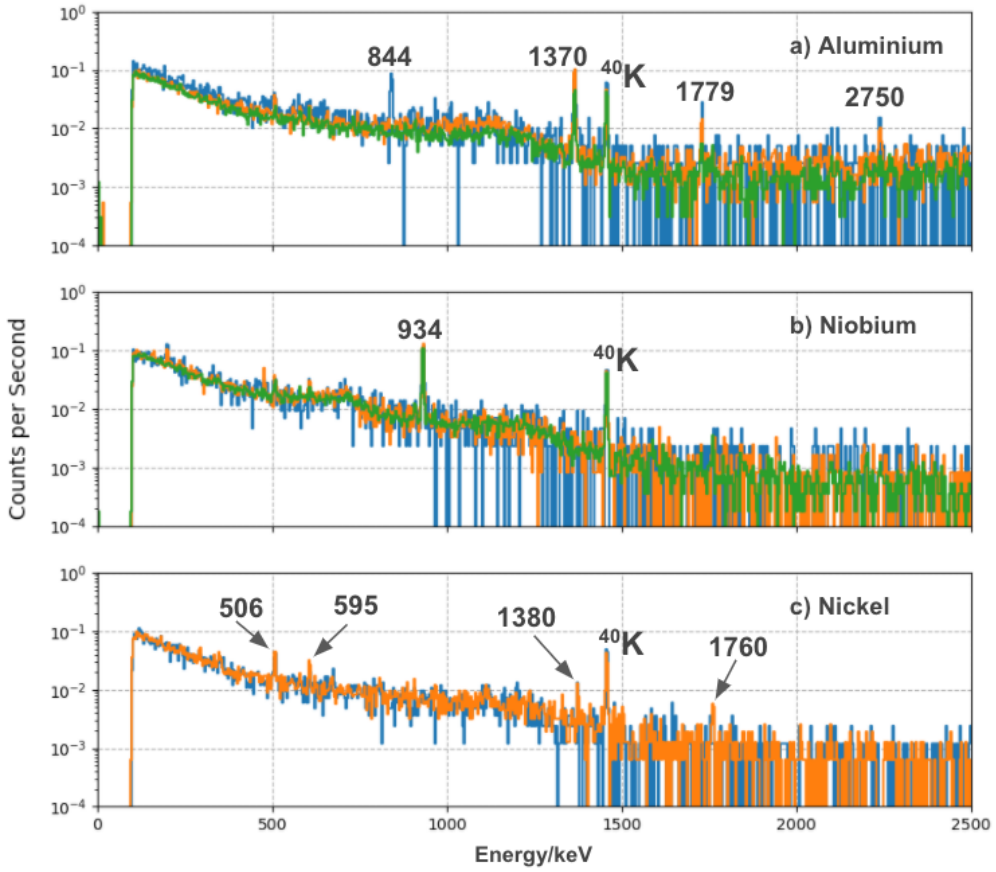

Figure 4.4: Aluminium, niobium and nickel foils measured in the LEPS detector at different intervals after irradiation has stopped: a) blue - 10 min, orange - 55 min, green - 17 h and 48 min, b) blue - 25 min, orange - 1 h 27 min, green - 20 h 43 min, c) blue - 10 min, orange - 55 min. Each spectrum has been rebinned from 0.4 keV/bin to 2 keV/bin due to low statistics.

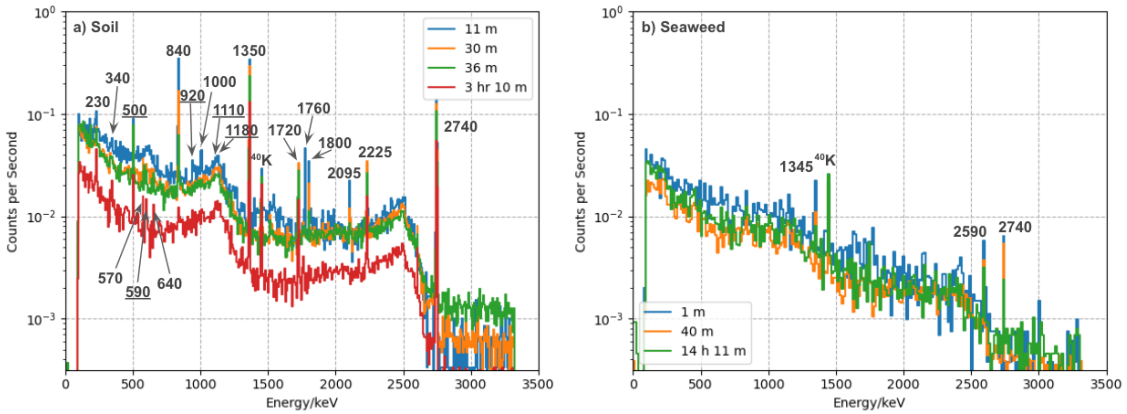

Figure 4.5: Environmental Samples: a) activated soil, b) activated seaweed. The time since irradiation stopped are stated in the legends. In a), data has been rebinned from 0.4 keV to 1.6 keV, and b) from 0.4 keV to 2 keV. The clearest peak energies have been labelled.

as well as several other peaks appearing from longer-lived activation products. These could be the decays resulting from In^{115}(n,2n)In^{114m} at 192, 558 and 724 keV with a half-life of 50 days. Peaks from background radiation [23] coming from 40K at 1461 keV and the 208Tl decay chain at 2615 keV also become more visible once the activity of the sample drops.

Fig 4.4 shows spectra measured from the aluminium, niobium and nickel foils after activation. Where possible, peaks have been matched to potential candidates for activation product decays. In a), the strongest peaks may correspond to ^{27}Mg at 844 keV, ^{24}Na at 1370 and 2750 keV and β-decay from ^{28}Si at 2750 keV. In b), the peak at 934 keV is likely to be from ^{92m}Nb. In C), the peaks at 1830 and 1760 keV may be from ^{57}Ni, and the 506 keV peak could be from annihilation. The peak at 595 keV was not matched to any known activation products.

The spectra resulting from the activated environmental samples is presented in Fig 4.5. The clearest peaks have been labelled with their energies. The underlined energies in the soil sample may correspond to the reaction ^{158}Gd(n,p)^{158}Eu, half-life 53 minutes. Reference values and intensities for this reaction are compared in table 4.1. The 500, 590 and 920 keV are shifted 20-30 keV, while the 1110 and 1120 keV peaks match up more closely. This is likely due to inaccuracies in the linear fit calibration, where a quadratic fit would have been more suitable. The count rate of the 1345 keV peak in the seaweed declines across the measurements, suggesting that this is a short-lived activation product. This is also seen in the 840, 2095, 1760 and 1800 keV peaks in the soil, however further analysis is required to identify reaction candidates for these and the other unknown peaks.

Table 4.1: Reference γ-ray energies and intensities for the reaction ^{158}Gd(n,p)^{158}Eu, half-life 53 minutes, compared with measured values in the soil sample.

Energy /keV	
Reference	**Measured**
520 (25%)	500
610 (8%)	590
950 (95%)	920
1110 (11%)	1110
1190 (16%)	1180

4.3 Short-term Irradiation with Pneumatic Transport System

4.3.1 Data Acquisition Systems

The CAEN VX1751 digitiser system allowed more than one detector to be used at once, and the high time resolution meant that coincidence measurements could be performed with precision. However, the files produced were several Gbs in size for measurements of only a few minutes, due to the full trace digitisation. This also lead to a high dead time of up to 99.9% in some measurements. As well as this, the 10 bit resolution produced much lower quality spectra than achievable with the LEPS DAQ. Furthermore, the raw data had to be processed and then analysed in python before it was possible to view the spectra. After processing several measurements, the very large data files and long analysis times rendered this DAQ unsuitable.

The CAEN DT5780 dual digital MCA proved to be the best DAQ. The main advantage was the superior dead time of only a few percent. A feature which allowed the plotting of waveforms and the display of live histogram data was also available. As well as this, having the bias supply and pre-amp power supply within the same box reduced signal noise from cables, producing the cleanest spectra of the three DAQs.

4.3.2 Detector Calibration

Energy and relative efficiency calibration was provided [41] for the two HPGe detector setup using the ^{152}Eu source and ENSDF reference data [23]. The resulting calibration curves are presented in Fig 4.6. The linear energy calibration is used for both detectors, however the data points in the efficiency are difficult to fit, due to anomalous points which are shown with the largest error bars.

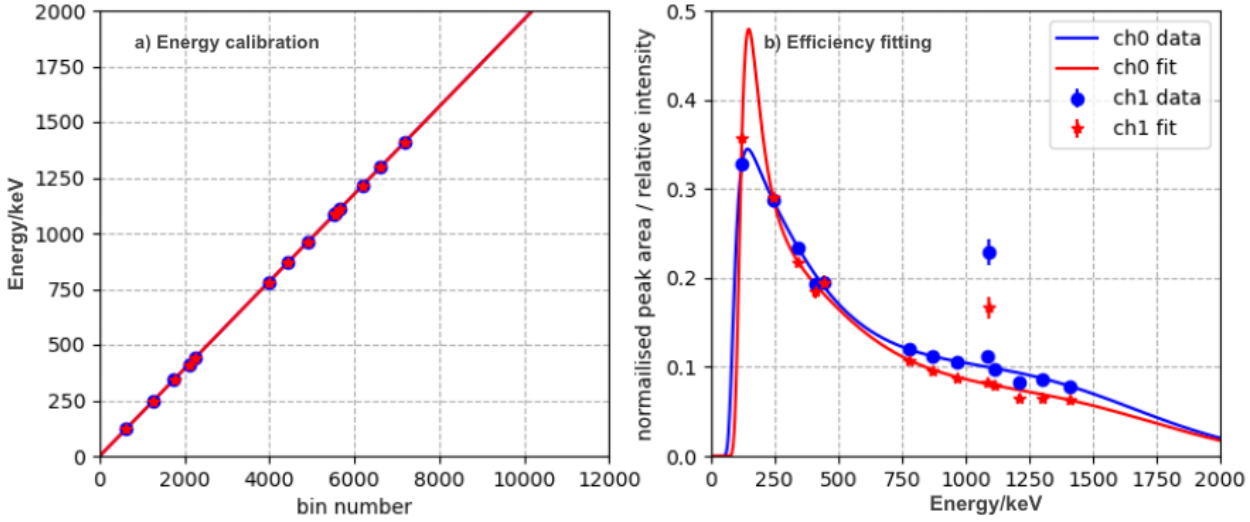

Figure 4.6: Double detector calibration: a) energy calibrated using a linear fitting, error bars are smaller than markers for data points; b) efficiency fitted with a seventh order polynomial in a loglog scale. Reference energies and intensities taken from ENSDF [23], calibration performed and provided by [41].

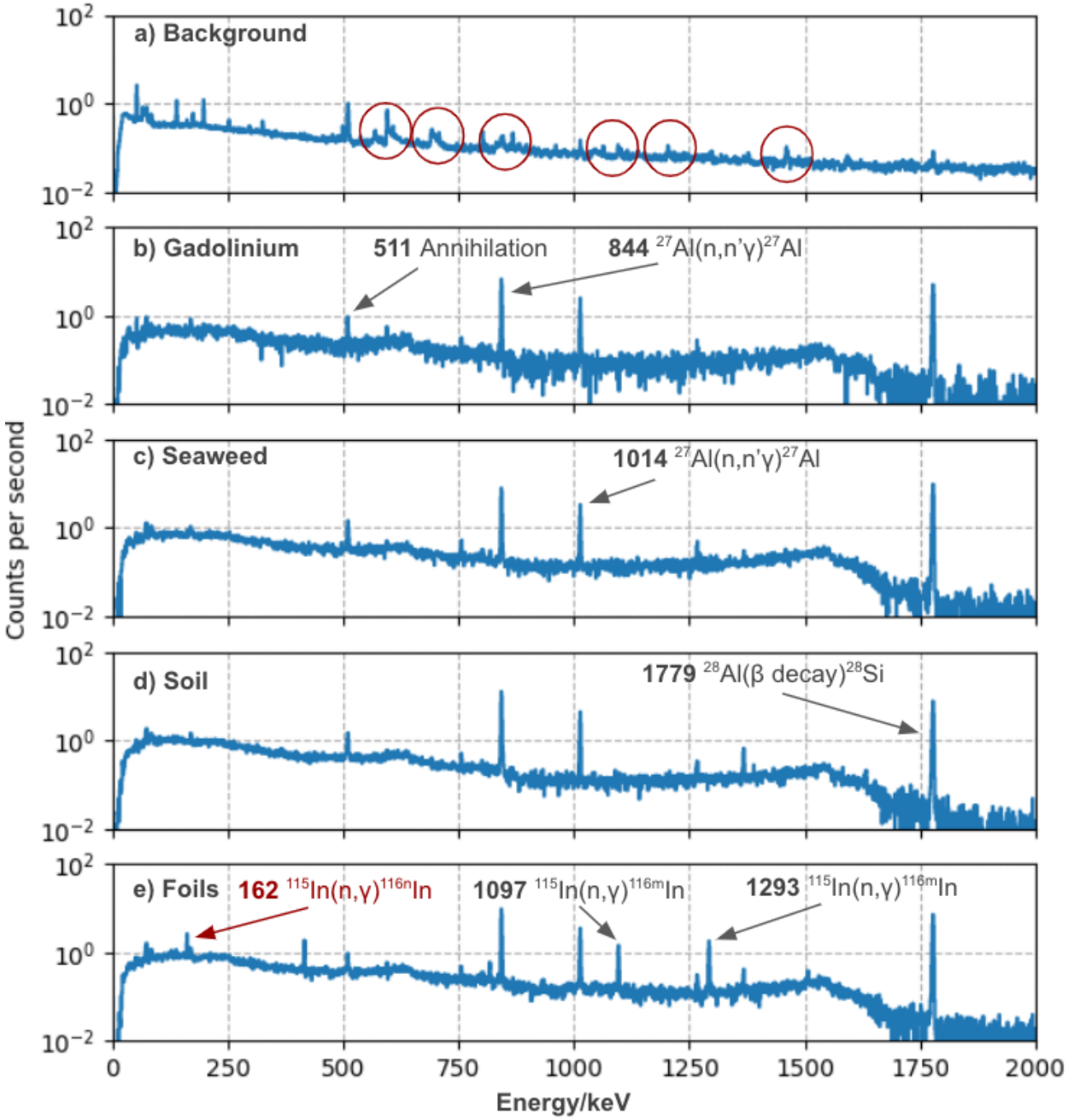

Figure 4.7: Spectra produced using the detector setup designed for fast pneumatic transport of samples. a) shows the background spectra, with triangular peaks from germanium recoils circled in red. b) shows that there is little activation in gadolinium. The peaks seen in this spectrum are also present in all others, resulting from activation of the aluminium sample holder. c) Seaweed: some peaks are seen, but are not strong enough to identify likely candidates at this stage. d) Soil: similarly, peaks are not strong enough to match with reference values. e) all foils irradiated together. The main peaks seen are from indium, including the 116mIn activation product with a half life of 2 seconds, highlighted in red.

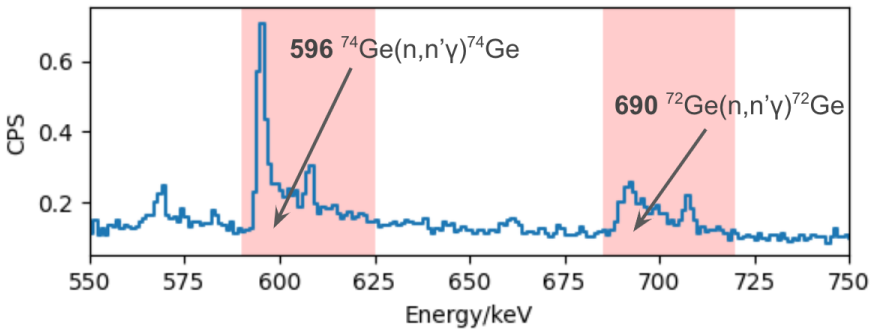

Figure 4.8: Triangular peaks seen in background spectrum resulting from the recoil of germanium nuclei with fast neutron scattering.

4.3.3 γ-ray Spectra

Fig 4.7 shows the spectra produced after each sample was irradiated using the pneumatic line. The peak at 162 keV in the lowest plot shows the activation of ^{115}In to ^{116n}In, the isomeric state with a 2 second half-life [28]. All of the peaks from the ^{116m}In reaction can be seen as well; the two largest peaks have been labelled here. The major peaks seen in all of the sample spectra originate from the reactions with aluminium in the sample holder. The background spectra highlights a feature of germanium activation by neutrons incident from the generator [42]. The circled peaks represent triangular γ-ray peaks, which result when a HPGe detector is exposed to neutrons of 1 MeV or greater. The peaks are produced by the sum of the recoil energy of germanium nuclei which have been deposited in the detector, and the photon energy emitted during relaxation of the nucleus which had been excited by inelastic scattering. Fig. 4.8 shows two of these peaks in more detail.

4.4 Comparison of Experimental and Calculated intensities

4.4.1 Calculation of Reaction Rate

The 2 second half-life and 54 minute half life activation products produced by irradiation of ^{115}In allowed a comparison of the two main methods of measurement. The reaction rates for the production of ^{116m}In and ^{116n}In were calculated according to equation 2.4. The product of the cross section and the neutron field shown in Fig 3.3, was multiplied by the number of atoms of ^{115}In present in the sample, which was $4.22 \cdot 10^{21}$ in the long-term irradiation. The foils were cut approximately in half after the three day irradiation period, so that one piece could be taken to Uppsala and one kept in Lund. The piece left in Lund contained $1.74 \cdot 10^{21}$, and was used in the fast pneumatic irradiation. The resulting plot for the energy dependent reaction rates is displayed in Fig 4.9. By integrating the reaction rates over all energies, the total number of reactions per minute were found and used in equations 2.3 and 2.5 to find the total number of atoms and expected activity at the time of measurement. It can be assumed that the number of target nuclei of ^{115}In is constant, because their depletion as a result of irradiation is negligible.

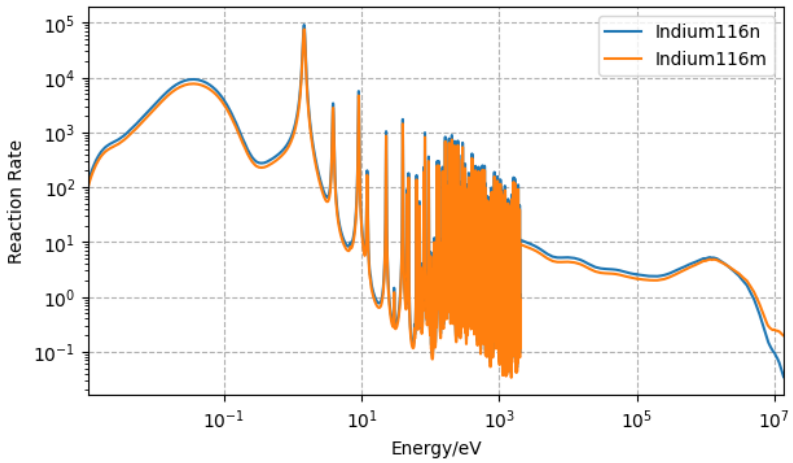

Figure 4.9: Reaction Rates for ^{116m}In and ^{116n}In as a function of energy, obtained by taking the product of the individual reaction cross sections with the simulated neutron flux.

4.4.2 Long-Term Irradiation

The calculated growth and decay of the ^{116m}In and ^{116n}In atoms during the three day irradiation is displayed in Fig 4.10. The measured and calculated results for the first two measurements of indium, represented by the red and purple regions in Fig. 4.10 b) are presented in Table 4.2 and 4.3. The measured counts were provided [41] and have been efficiency corrected, and the statistical uncertainties based on the covariance matrix from the peak fitting. The calculated counts were generated through the model used in Fig. 4.10, and scaled to the known intensities of each of the peaks and solid angle. Calculated uncertainties were based on an uncertainty in time of 2 minutes, with this assumed to be the dominant uncertainty. Because this was a parasitic experiment, the irradiation stop time was not recorded exactly as this was not of concern to the main experiment. As well as this, the clocks on the PCs in the LIBAF hall were not matched, and it is not known which clock was referenced for the stop time of the NG.

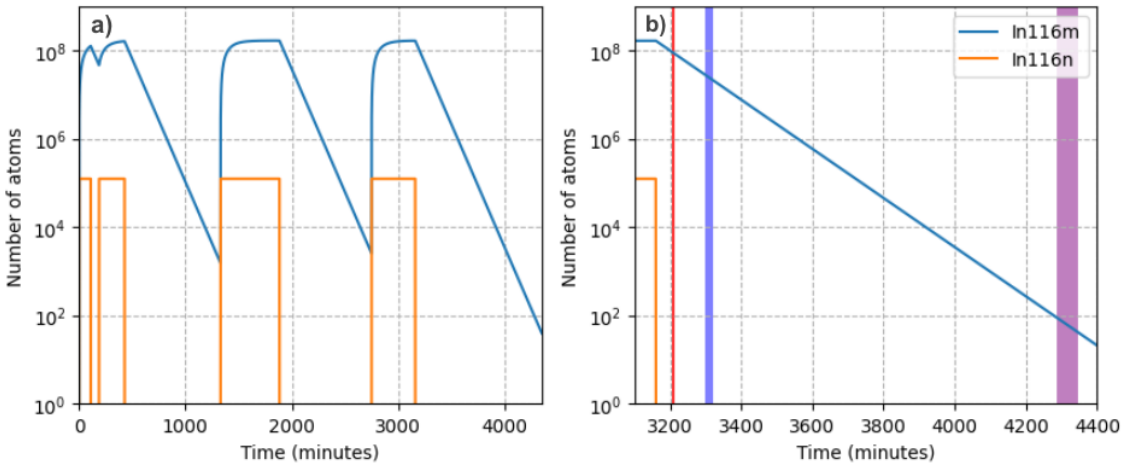

Figure 4.10: a) The calculated growth and decay of ^{116m}In (blue) and ^{116n}In (orange) atoms over 4500 minutes during long-term irradiation. b) shows the period following irradiation when measurements were taken. The red, blue and purple shaded sections denote when measurement occurred.

Table 4.2: ^{116m}In first long-term measurement, measured and calculated counts. Measured counts have been efficiency corrected. Calculated counts were scaled to the known intensities of each of the peaks and solid angle. Errors are based on an uncertainty in time of 2 minutes.

First Measurement		
Energy/keV	**Measured**	**Calculated**
138.06	146.23 +/- 9.44	212.55 +/- 48.52
355.29	23.01 +/- 2.1	40.21 +/- 9.57
416.86	829.5 +/- 34.13	1562.55 +/- 356.72
463.33	20.91 +/- 2.61	40.21 +/- 9.51
511.21	20.85 +/- 2.32	-
818.68	358.14 +/- 11.8	696.83 +/- 159.08
1097.19	1747.05 +/- 56.99	3360.64 +/- 767.2
1293.45	2518.23 +/- 71.71	4871.49 +/- 1112.11
1507.47	338.37 +/- 9.61	569.87 +/- 130.1
1752.19	95.53 +/- 5.81	135.57 +/- 30.95
2111.98	958.24 +/- 29.3	867.45 +/- 197.9

The calculated CPS are approximately twice the value of the measured CPS in both measurements. This may be because the neutron energy spectrum was simulated at the end of the collimator at a distance of 22.5 cm from the target, where the neutrons would be much more moderated by interactions with surrounding material. In reality the foils were placed at a distance of 5.5 cm from the target, where neutron energies will largely be 14 MeV. Despite the slightly lower neutron flux at a further distance, the reaction rate at 14 MeV is up to 10^3 times lower for ^{115}In than for thermal neutrons. This would overestimate the reaction rate, based on the fact that the simulation models more neutrons at thermal energies with a higher cross section than in reality.

Table 4.3: ^{116m}In second measurement, measured and calculated counts. Measured counts have been efficiency corrected. Calculated counts were scaled to the known intensities of each of the peaks and solid angle. Errors are based on an uncertainty in time of 2 minutes.

Second Measurement		
Energy/keV	**Measured**	**Calculated**
137.83	34.83 +/- 1.9	65.63 +/- 51.28
335.66	4.32 +/- 0.37	-
355.03	5.52 +/- 0.41	12.42 +/- 10.12
416.57	226.32 +/- 10.92	482.48 +/- 376.99
462.94	6.19 +/- 0.75	12.42 +/- 10.05
510.5	4.83 +/- 0.62	-
818.34	99.59 +/- 3.98	215.17 +/- 168.12
1096.86	473.57 +/- 15.68	1037.69 +/- 810.81
1293.12	676.85 +/- 22.16	1504.21 +/- 1175.33
1507.05	90.19 +/- 3.06	175.96 +/- 137.49
1751.76	27.16 +/- 1.14	41.86 +/- 32.71
2111.61	252.41 +/- 7.36	267.85 +/- 209.15

4.4.3 Short-Term Irradiation

Fig 4.11 shows the growth of atoms in the pneumatic activation of the foils. Table 4.4 presents the measured and calculated counts for the single ^{116n}In peak at 162 keV, and the two strongest peaks of ^{116m}In. The solid angle was calculated based on the same detector crystal documented in the manual for LEPS detector as there was no documentation available for either of the detectors.

Table 4.4: ^{116m}In and ^{116n}In measured and calculated counts for the short-term irradiation experiment. Measured counts have been efficiency corrected. Calculated counts were generated and scaled to the known intensities of each of the peaks and solid angle of both detectors. Uncertainties were calculated based on an uncertainty of 1 second in the measurement start and end times.

	Energy/keV	**CPS measured**	**CPS calculated**
^{116n}In	161.89	5.29 +/- 3.49	45.09 +/- 17.32
^{116m}In	1096.78	23.29 +/- 3.36	66.21 +/- 5.15
^{116m}In	1293.06	36.37 +/- 3.62	96.21 +/- 7.48

Similarly, the greatest error in the calculated counts arises from the uncertainty in time. The time taken between each irradiation and measurement was measured by looking at a digital clock, estimating to the nearest second, while times for the measured counts were recorded by the CAEN software. Given that the half life of ^{116n}In is 2 seconds, a 1 second discrepancy in the time stamps results in a large difference in the number of atoms measured vs calculated.

As well as this, the NG was considered 'off' as soon as the switch was flicked to transport the sample to the detectors. In the model used to produce the data shown in Fig.4.11, this meant swapping directly from equation 2.1.3 to 2.1.5. In reality, the sample may still be activating during the time that it travels away from the neutron source. The uncertainty in activation has not been accounted for in error propagation. The sample holder also became

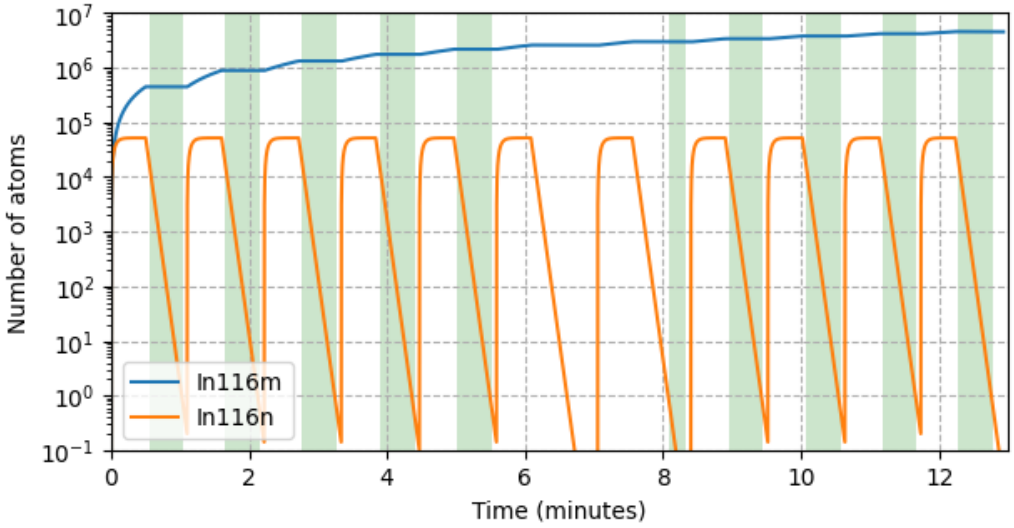

Figure 4.11: The calculated growth and decay of ^{116m}In (blue) and ^{116n}In (orange) atoms over 13 minutes during the short-term irradiation experiment. The green shaded sections denote when measurement occurred.

trapped in the hose between 5.5 and 8 minutes. Its position has been estimated but is not known; it may have been considered to be irradiating when in fact it was not. This is another factor which would increase the number of calculated counts.

The uncertainty in activation increases exponentially with time, particularly in isotopes with longer half lives which do not decay entirely within the time between activations. This is because the number of atoms from the previous activation N_0 feeds into the following decay equation. On the other hand, statistical uncertainty decreases exponentially over time as the number of counts increases. With more time, covariance plots could have been generated to visualise the uncertainties arising from inaccurate time-stamping. By modelling both activation and statistical uncertainties, it would be possible to calculate the optimal measurement time for each reaction to minimise uncertainty.

Uncertainties in the measured counts may be the result of inaccurate detector efficiency fitting. The fit below energies of 250 keV fails to replicate realistic values in this region, making it unreliable. The sudden drop here could account for the even lower measured to calculated counts ratio for the ^{116m}In than for the ^{116m}In counts. This fitting was used because it was still more realistic than using no fitting at all, but this is something that should be redone with additional data points in future.

5 Summary and Outlook

This project established the first stages of the development of the NAA station at LIBAF. In this initial phase, the focus was to facilitate the measurement of very short-lived activation products, and determine the feasibility of measuring environmental samples with the methods used.

5.1 Conclusions

Strong activation was seen in the soil sample with long-term irradiation, which could be the result of the presence of the most abundant isotope of gadolinium, ^{158}Gd. Peaks were identified at energies of 500, 590, 920, 1110 and 1180 keV, and were matched to the energies of the ^{158}Eu activation product with a half-life of 53 minutes. The measured energies were shifted approximately 20-30 keV, and this is likely due to inaccuracies in the linear fit calibration.

The Indium foil also became strongly activated in both the long and short-term irradiation setups, and peaks from the ^{116m}In and ^{116n}In known activation products were examined. The counts measured by the detector were compared with results calculated using simulations of the neutron field and reaction cross sections. In the long-term measurements, the calculated and measured results were within two standard deviations. The short term results showed greater discrepancies between the measured and calculated counts, and were approximately 5 standard deviations apart. This is due to increased sources of error arising from the short irradiation and measurement times, which were manually time-stamped.

Using the two different methods of short and long term measurement, a comparison could be drawn between the utility of each type. Activation in environmental samples was not seen in the pneumatic setup because of the limitations of the geometry; the current configuration requires the sample to fit into a container in order to be transported in the hose. However, the identification of the ^{116n}In peak with a 2 second half life using the pneumatic line demonstrated the success of this system for capturing the presence of short lives radionuclides. Improvements are required to make this measurement station suitable for quantitative identification of radionuclides in environmental samples; some suggestions are included in the following section. Despite this, the results produced at this initial stage are a promising starting point for continued development of the station for use with the LIBAF CANS.

5.2 Further Work

For future development, a method of more effectively compressing the environmental samples could be implemented to fit the maximum mass into the container to improve the likelihood of activation. It was noticed that the seaweed sample showed significantly less activation than the soil sample, even when taking into account the smaller sample size. This may

suggest that pre-concentration or pre-separation methods are required to see better results, or higher neutron flux. Further work could also focus on identifying the unknown peaks in these samples and compare them with those already identified by the BAR group.

The greatest source of error in these experiments arose from time-stamping. In the pneumatic system, the implementation of a sensor limit switch at each end of the pneumatic system could automate the transport and measurement and recording time stamps automatically, and would reduce the measurement errors significantly.

Acknowledgements

I would like to acknowledge several people in the nuclear physics at Lund who have so kindly taken the time to help me get started and guide me along the way. In particular, Mikael Elfman, who spent many hours helping with the project in the lab, as well as Nicholai Mauritzson, and Markus Kristensson who have also been very accommodating of me. Kristina Stenström has been a supportive co-supervisor and very knowledgeable point of contact for me.

At the beginning of my project, Mattias Lantz from Uppsala University helped me to become familiarised with activation analysis, and he together with Johanna Brodin were happy to share data with me from their calculations in FISPACT II.

I have some very helpful friends who have been kind enough to assist when I have had questions about programming, and I would like to thank Javier Morales and Markus Höglin for this especially.

I would finally like to thank my supervisor, Robert Frost, who has been unfailingly patient with me, and guided me through what has been a challenging and very rewarding project. I cannot thank him enough for the time he has put in to make sure I get the most of this experience.

References

[1] P. Kruger. *Principles of activation analysis, Ch 3.* John Wiley & Sons, Inc., 1971.

[2] K. Stenström, V. Barkauskas, G. P. Hiaa, C. Nilsson, C. Rääf, H. Holstein, S. Mattsson, J. Martinsson, M. Jönsson, and C. Bernhardsson. Identifying radiologically important ESS-specific radionuclides and relevant detection methods, Swedish Radiation Authority, 2020.

[3] K. Waldner, L. Waldner, S. Mattsson, K. E. Stenström, M.Jönsson, C. Bernhardsson, G. P. Hiaa, and C.Rääf. Assessment of "Zero Point" radiation around the ESS facility, Lund University. 2019.

[4] G. F. Knoll. *Radiation detection and measurement, Ch 8.* Wiley, 2010.

[5] H. Tsukada, A. Takeda, H. Hasegawa, S. Ueda, and T. Iyogi. Comparison of NAA and ICP-MS for the determination of major and trace elements in environmental sample. *Journal of Radioanalytical and Nuclear Chemistry*, 263(3):773–778, feb 2005.

[6] E. Witkowska, K. Szczepaniak, and M. Biziuk. Some applications of neutron activation analysis. *Journal of Radioanalytical and Nuclear Chemistry*, 265, 6 2005.

[7] T. C. M. Matsubara, M. Saiki, and G. S. Zahn. Investigating the antimony determination in environmental samples by NAA. *Journal of Radioanalytical and Nuclear Chemistry*, 291, 1 2012.

[8] P. J. Potts. *A handbook of silicate rock analysis: Ch. 12, Neutron activation analysis.* Springer Netherlands, 1987.

[9] P. Kruger. *Principles of activation analysis, Ch 7.* John Wiley & Sons, Inc., 1971.

[10] Z.Alfassi. *Activation analysis, Ch 1.* CRC Press, 1990.

[11] S. Boschi, B. Schmitz, F. Terfelt, L. Ros, M. Elfman, P. Kristiansson, C. Sulas, S. Monechi, and A. Montanari. Popigai impact ejecta layer and extraterrestrial spinels recovered in a new italian location—the monte vaccaro section (marche apennines, italy), geological society of america. pages 355–367, 2019.

[12] A. S. Krane. *Introductory nuclear physics, Ch 6.* Wiley, 1987.

[13] J. Chadwick. The existence of a neutron. *Proceedings of the Royal Society of London. Series A, Containing Papers of a Mathematical and Physical Character, The Royal Society*, 136:692–708, 6 1932.

[14] J. Lilley. *Nuclear physics, Ch 1.* John Wiley & Sons Inc, 2001.

[15] A. S. Krane. *Introductory nuclear physics, Ch 13.* Wiley, 1987.

[16] C. F. v. Weizsäcker. Zür theorie der kernmassen, Springer Science and Business Media LLC. *Zeitschrift für Physik*, 96(7-8):431–458, 7 1935.

[17] A. S. Krane. *Introductory nuclear physics, Ch 3.* Wiley, 1987.

[18] J. Lilley. *Nuclear physics, Ch 2.* John Wiley & Sons Inc, 2001.

[19] O. Sorlin and M.-G. Porquet. Nuclear magic numbers: New features far from stability. *Progress in Particle and Nuclear Physics, Elsevier BV*, 61:602–673, 10 2008.

[20] D. Reilly, N. Ensslin, and H. Jr. Smith. Passive nondestructive assay of nuclear materials, United States, 1991.

[21] A. S. Krane. *Introductory nuclear physics, Ch 12.* Wiley, 1987.

[22] J. Lilley. *Nuclear physics, Ch 3.* John Wiley & Sons Inc, 2001.

[23] A. J. M. Plompen, O. Cabellos, C. De Saint Jean, M. Fleming, A. Algora, M. Angelone, P. Archier, E. Bauge, O. Bersillon, A. Blokhin, F. Cantargi, A. Chebboubi, C. Diez, H. Duarte, E. Dupont, J. Dyrda, B. Erasmus, L. Fiorito, U. Fischer, D. Flammini, D. Foligno, M. R. Gilbert, J. R. Granada, W. Haeck, F.-J. Hambsch, P. Helgesson, S. Hilaire, I. Hill, M. Hursin, R. Ichou, R. Jacqmin, B. Jansky, C. Jouanne, M. A. Kellett, D. H. Kim, H. I. Kim, I. Kodeli, A. J. Koning, A. Yu. Konobeyev, S. Kopecky, B. Kos, A. Krása, L. C. Leal, N. Leclaire, P. Leconte, Y. O. Lee, H. Leeb, O. Litaize, M. Majerle, J. I Márquez Damián, F. Michel-Sendis, R. W. Mills, B. Morillon, G. Noguère, M. Pecchia, S. Pelloni, P. Pereslavtsev, R. J. Perry, D. Rochman, A. Röhrmoser, P. Romain, P. Romojaro, D. Roubtsov, P. Sauvan, P. Schillebeeckx, K. H. Schmidt, O. Serot, S. Simakov, I. Sirakov, H. Sjöstrand, A. Stankovskiy, J. C. Sublet, P. Tamagno, A. Trkov, S. van der Marck, F. Álvarez Velarde, R. Villari, T. C. Ware, K. Yokoyama, and G. Žerovnik. The joint evaluated fission and fusion nuclear data library, JEFF-3.3. *The European Physical Journal A*, 56, 7 2020.

[24] O. Haxel, J. Hans D. Jensen, and H. E. Suess. On the "magic numbers" in nuclear structure. *Physical Review*, 75, 6 1949.

[25] J. Lilley. *Nuclear physics, Ch 10.* John Wiley & Sons Inc, 2001.

[26] K. Hirota, G. Ichikawa, M. Kitaguchi, Y. Kiyanagi, H.M. Shimizu, K. Tsuchida, A. Uritani, and K. Watanabe. Development of Accelerator-driven Compact Neutron Sources, Nagoya University, Nagoya. 2018.

[27] F.Ott, A. Menelle, and C. Alba-Simionesco. The SONATE project, a French CANS for materials sciences research. *EPJ Web of Conferences*, 231, 3 2020.

[28] M. R. Bhat. *Evaluated Nuclear Structure Data File (ENSDF).* 1992.

[29] R. Garoby, A. Vergara, H. Danared, I. Alonso, E. Bargallo, B. Cheymol, C. Darve, M. Eshraqi, H. Hassanzadegan, A. Jansson, I. Kittelmann, Y. Levinsen, M. Lindroos, C. Martins, Ø. Midttun, R. Miyamoto, S. Molloy, D. Phan, A. Ponton, E. Sargsyan, T. Shea, A. Sunesson, L. Tchelidze, C. Thomas, M. Jensen, W. Hees, P. Arnold, M. Juni-Ferreira, F. Jensen, A. Lundmark, N. Gazis, J. Weisend, M. Anthony, E. Pitcher, L. Coney, M. Göhran, J. Haines, R. Linander, D. Lyngh, U. Oden, H. Carling, R. Andersson, S. Birch, J. Cereijo, T. Friedrich, T. Korhonen, E. Laface, M. Mansouri-Sharifabad, A. Monera-Martinez, Nordt, D. Paulic, D. Piso, S. Regnell, M. Zaera-Sanz, M. Aberg, K. Breimer, K. Batkov, Y. Lee, L. Zanini, M. Kickulies, Y. Bessler,

J. Ringnér, J. Jurns, A. Sadeghzadeh, P. Nilsson, M. Olsson, J.-E. Presteng, H. Carlsson, A. Polato, J. Harborn, K. Sjögreen, G. Muhrer, and F. Sordo. Corrigendum: the European Spallation Source design. *Physica Scripta*, 93, 12 2018.

[30] J.W.G. Thomason. The ISIS spallation neutron and muon source—the first thirty-three years. *Nuclear Instruments and Methods in Physics Research Section A: Accelerators, Spectrometers, Detectors and Associated Equipment*, 917, 2 2019.

[31] J. Lilley. *Nuclear physics, Ch 5.* John Wiley & Sons Inc, 2001.

[32] A.H. Compton. A quantum theory of the scattering of X-rays by light elements. *Physical Review*, 21, 5 1923.

[33] G. F. Knoll. *Radiation detection and measurement, Ch 12.* Wiley, 2010.

[34] A. S. Krane. *Introductory nuclear physics, Ch 7.* Wiley, 1987.

[35] J. Lilley. *Nuclear physics, Ch 6.* John Wiley & Sons Inc, 2001.

[36] G. F. Knoll. *Radiation detection and measurement, Ch 2.* Wiley, 2010.

[37] M.Oshima, Y. Toh, Y. Hatsukawa, T. Hayakawa, and N. Shinohara. A high-sensitivity and non-destructive trace element analysis based on multiple gamma-ray detection. *Journal of Nuclear Science and Technology*, 39, 4 2002.

[38] C. Bedouet. *GENIE 16NG user manual, MU_ 00002098.* SODERN, 2014.

[39] M. Kristensson. Private communication, Lund University, Sweden, 2020.

[40] M. Baginova, P.Vojtyla, and P. P. Povinec. Investigation of neutron interactions with Ge detectors. *Nuclear Instruments and Methods in Physics Research Section A: Accelerators, Spectrometers, Detectors and Associated Equipment*, 897, 7 2018.

[41] R.J.W. Frost. Private communication, Lund University, Sweden, 2020.

[42] E. Gete, D. F. Measday, B. A. Moftah, M. A. Saliba, and T. J. Stocki. Neutron-induced peaks in Ge detectors from evaporation neutrons. *Nuclear Instruments and Methods in Physics Research Section A: Accelerators, Spectrometers, Detectors and Associated Equipment*, 388, 3 1997.